

Restructuring dynamics of surface species in bimetallic nanoparticles probed by modulation excitation spectroscopy

Received: 9 January 2024

Accepted: 29 July 2024

Published online: 07 August 2024



Prahlad K. Routh¹, Evgeniy Redekop², Sebastian Proding²,
Jessi E. S. van der Hoeven³, Kang Rui Garrick Lim^{4,5}, Joanna Aizenberg^{4,5},
Maarten Nachtegaal⁶, Adam H. Clark⁶ & Anatoly I. Frenkel^{1,7}✉

Restructuring of metal components on bimetallic nanoparticle surfaces in response to the changes in reactive environment is a ubiquitous phenomenon whose potential for the design of tunable catalysts is underexplored. The main challenge is the lack of knowledge of the structure, composition, and evolution of species on the nanoparticle surfaces during reaction. We apply a modulation excitation approach to the X-ray absorption spectroscopy of the 30 atomic % Pd in Au supported nanocatalysts via the gas (H_2 and O_2) concentration modulation. For interpreting restructuring kinetics, we correlate the phase-sensitive detection with the time-domain analysis aided by a denoising algorithm. Here we show that the surface and near-surface species such as Pd oxides and atomically dispersed Pd restructured periodically, featuring different time delays. We propose a model that Pd oxide formation is preceded by the build-up of Pd regions caused by oxygen-driven segregation of Pd atoms towards the surface. During the H_2 pulse, rapid reduction and dissolution of Pd follows an induction period which we attribute to H_2 dissociation. Periodic perturbations of nanocatalysts by gases can, therefore, enable variations in the stoichiometry of the surface and near-surface oxides and dynamically tune the degree of oxidation/reduction of metals at/near the catalyst surface.

The surface species of nanoparticle alloys are responsible for the tunability of optical, plasmonic, sensing and catalytic properties which differ dramatically from their monometallic or bulk counterparts^{1,2}. In heterogeneous catalysts, for example, the knowledge of structural and compositional changes during reaction conditions is sought for understanding the reaction mechanisms and for steering in-situ catalyst restructuring towards better-performing surface configurations,

as well as for identifying catalyst deactivation pathways and subsequent mitigation strategies^{3–5}. However, direct experimental monitoring of dynamic changes in the structure of catalysts is very challenging, given the multiple forms of heterogeneity of the active sites and the scarcity of techniques suitable for monitoring the dynamic evolution of the catalytically active species on the catalyst surfaces under the reaction conditions⁶. In bimetallic nanocatalysts,

¹Department of Materials Science and Chemical Engineering, Stony Brook University, Stony Brook, NY 11794, USA. ²Centre for Materials Science and Nanotechnology (SMN), Department of Chemistry, University of Oslo, N-0315 Oslo, Norway. ³Materials Chemistry and Catalysis, Debye Institute for Nanomaterials Science, Utrecht University, 3584 CG Utrecht, The Netherlands. ⁴Harvard John A. Paulson School of Engineering and Applied Sciences, Harvard University, Cambridge, MA 02138, USA. ⁵Department of Chemistry and Chemical Biology, Harvard University, Cambridge, MA 02138, USA. ⁶Paul Scherrer Institut (PSI), Villigen CH-5232, Switzerland. ⁷Division of Chemistry, Brookhaven National Laboratory, Upton, NY 11973, USA.

✉ e-mail: anatoly.frenkel@stonybrook.edu

dynamic changes may include the formation and interconversion of various surface ensembles (e.g., monomers, dimers, and trimers in dilute regimes⁷) in response to the catalyst pretreatments conditions; the segregation of alloyed, monometallic, or oxide regions (islands) at the catalyst surface⁸, and the formation of intermediate species⁹ depending on the external stimuli and the reaction conditions^{10,11}.

Bimetallic Pd-Au nanocatalysts¹², which possess dual functionality with a minority metal (Pd) as the active element and a majority element (Au) as a less reactive host matrix that imparts selectivity^{13,14}, have been shown to exhibit changes in the coverage and nature of surface metal species as a result of e.g., oxidative^{15,16} and reductive environment^{7,11}. Despite enormous interest^{14,17}, the changes under dynamic conditions were studied primarily by either focusing on a small subset of particles (by using in-situ electron energy loss spectroscopy (EELS) and high-resolution transmission electron microscopy (HRTEM)⁸) or on the basis of planar model systems¹⁸. X-ray absorption spectroscopy (XAS) can potentially unlock the details of structure and dynamics in nanoparticles under realistic temperature and pressure conditions due to its elemental specificity, local structure sensitivity (interatomic bond lengths can be measured with an accuracy of 0.01 Å or better), and excellent time resolution (the duration of XAS snapshot of the local coordination is of the order of 1 fs). However, XAS probes the entire structure of the nanoparticle and, therefore, is dominated by the atoms in the interior (spectators), while the catalytic action engages the minority of the atoms (active species) located at the surface or subsurface¹⁹. In “spectators” we also include the species that react to the changing gas conditions at much longer times than the gas switching times used in our experiments. Modulation excitation, coupled with time-resolved XAS (ME-XAS), can significantly enhance the sensitivity towards active species^{20,21}. During the ME-XAS process, a periodic perturbation (stimulus), such as gas composition change, is applied to a catalytic sample as shown schematically in Fig. 1. The periodic XAS response of active species, which appears in sync with the applied periodic stimulus, can be selectively separated from the total signal (dominated by spectators) by post-processing the time-

dependent data using a phase-sensitive detection (PSD)^{20,21}. Hence, demodulated ME-XAS signal corresponds only to changes in the active species. Moreover, this demodulated signal varies as a function of phase delay from periodic stimulus and, therefore, it encodes the kinetic information^{22–24}. Ferri et al.^{23,25} have shown that maxima in the demodulated signal in the extended X-ray absorption fine structure (EXAFS) range can be analyzed using conventional Fourier transform procedure and thus obtained EXAFS fitting parameters reveal details about the local structure, identity and kinetics of surface species (active component in our bimetallic catalyst), although previous attempts to analyze it were limited to the monometallic catalysts only^{26–28}.

Herein, we examine 30 atomic % Pd-Au bimetallic nanoparticles (ca. 7.0 nm in diameter) embedded in a SiO₂ support, featuring markedly heterogeneous distribution of Pd atoms within Au host, ranging from three-dimensional Pd-rich regions to surface Pd_nAu (n = 1, 2, or 3) ensembles. As such, this system is an excellent candidate for applying the ME-XAS for studying the kinetics of restructuring of bimetallic components near/at the nanoparticle surfaces. Figure 1 provides a schematic of our approach, which shows periodic application of stimuli in the form of alternating gaseous atmosphere (at a fixed frequency) in a reactor containing the 30% Pd-Au bimetallic nanoparticles. For gas modulation, we chose H₂ and O₂ as two gases that can induce multiple possible changes in the structure and electronic properties of Pd atoms at 250 °C. The changes may include formation and decomposition of Pd_nAu ensembles^{7,29}, Pd clusters^{8,30}, Pd hydrides³⁰ and/or oxides³¹. The ability to separate between these, likely, coexisting processes, and characterize them individually is a key capability needed for studying a large class of bimetallic materials that restructure heterogeneously during reactions or processes. The EXAFS portion of the demodulated spectra revealed the identity and structure of the surface and near-surface species, Pd-rich regions (as shown by the shell of surface atoms after demodulation in Fig. 1), while phase delays in the demodulated X-ray absorption near-edge structure (XANES) spectra provided insights into their restructuring kinetics.

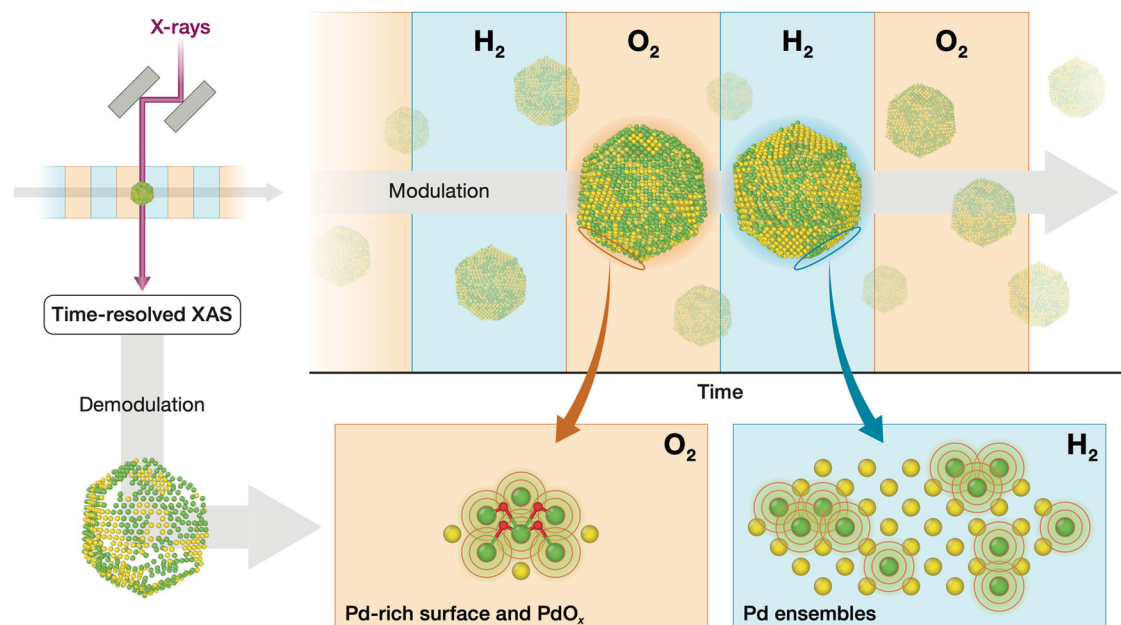


Fig. 1 | Schematic of modulation excitation coupled with XAS (ME-XAS). The system is subjected to periodic stimulation by changes in the gas atmosphere. Time-resolved XAS spectra from active and spectator species are captured with gas modulation. The demodulation of time-resolved XAS signals results in separation of signals from active and spectator species and the former is further used for their

quantitative analysis. Concentration modulation of the gas atmosphere using periodic pulse of 60 s–long 20% H₂ (in He) and 60 s–long 20% O₂ (in He) gas pulses, shown in blue and orange regimes respectively, with a total period of 120 s, while collecting Pd K-edge X-ray absorption spectra with 0.5 s time-resolution.

The time-resolved evolution of surface and near-surface species identified as the heterogeneous mixture of Pd-rich islands, provides information on their restructuring in bimetallic nanocatalyst systems.

Results

Identification of restructuring surface species

The signal to noise ratio of XAS can be significantly enhanced by averaging over many repeated cycles of modulated excitation resulting in one effective period of modulation representing the time-dependent changes by reducing stochastic noise. Such averaging is commonly referred to as “event-averaging”³² for non-periodic but identical events and “period-averaging” for periodic and identical perturbations. Figure 2a highlights that the most significant changes due to different gas environments in the XANES region after “period-averaging” over 50 cycles, indicating a potential change in Pd oxidation state and Pd oxide formation^{33,34}. However, the restructuring of Pd-Au atoms can also exhibit similar effects on the spectral shape in the XANES region⁷. In fact, there is a plethora of possibilities which can explain the observed changes in time-resolved XANES. Small Pd_nAu ensembles ($n = 1-3$) can form and dissolve in O₂ and H₂ environments, respectively, as reported recently in dilute Pd in Au alloys^{7,29}. Another possibility is periodic formation of Pd oxide species during O₂ pulse and their subsequent decomposition in H₂ pulse, as indicated by the presence of a Pd-O scattering contribution in the EXAFS of Pd-Au treated in O₂ atmosphere as well as O₂ treatment of pure-Pd (i.e., monometallic) nanocatalysts²³. In the case of Pd-Au bimetallic nanoparticles with higher Pd fraction (such as 25% Pd-Au), Pd atoms are also shown to cluster in the presence of O₂³⁰. Conventional EXAFS analysis of the period-averaged spectra, despite the substantially improved signal to noise ratio is not practical for this class of materials with minority active species because the EXAFS spectra are dominated by the spectator Pd atoms inside the nanoparticles. To illustrate this, Fig. 2b depicts continuous Cauchy wavelet transform (WT) representation of the “period-averaged” EXAFS data at the end of O₂ half

cycle ($t = 60$ s). WT provides a simultaneous representation of EXAFS signal in k -space and r -space³⁵. In Fig. 2b, only Pd-Pd and Pd-Au scattering paths can be identified, with no indications of Pd-O scattering, despite corresponding to the peak of the oxidizing atmosphere within the period.

The PSD procedure, described by an equation:

$$\mu^{\text{PSD}}(E) = \frac{2}{T} \int_0^T \mu(E, t) \sin(\omega t + \phi_{\text{PSD}}) dt, \quad (1)$$

in which the modulation period T (in our case, $T = 120$ s), produces a difference spectrum parameterized in terms of the phase angle (ϕ_{PSD}), i.e., a spectrum corresponding to the ensemble-averaged catalyst from which the contribution of spectators in the interior of the nanoparticle was subtracted (i.e., corresponding to a remaining “hollow” bimetallic shell shown schematically in Fig. 1). In the first-order approximation, the PSD spectrum can be represented by the difference spectrum for two structural models corresponding to the limiting states of the restructuring process, whose difference can account for residual scattering signals observed in demodulated spectra. With Pd oxide as the dominant species during O₂ pulse, a difference between Pd oxide reference spectrum and Pd-Au spectrum after the modulation (they were chosen as such “limiting” models), shown by the dotted line in Fig. 2c, has a good “in-phase” agreement with the demodulated XANES. Hence, the formation of PdO_x in O₂ and subsequent decomposition in H₂ half cycle is proposed as the primary structural model during modulation. Supplementary Note 1 shows an analytical relationship between the fraction of “active” species and μ^{PSD} . Using that formalism, we estimate from the maxima of μ^{PSD} that approximately 7% of the species undergo oscillations with the frequency of gas modulation, i.e., 7% Pd atoms belong to the active species.

The WT of the demodulated EXAFS spectra (Fig. 2d) at the phase angle $\phi_{\text{PSD}} = 144^\circ$ corresponding to the phase angle with the highest contrast in the demodulated EXAFS spectra, clearly shows a scattering

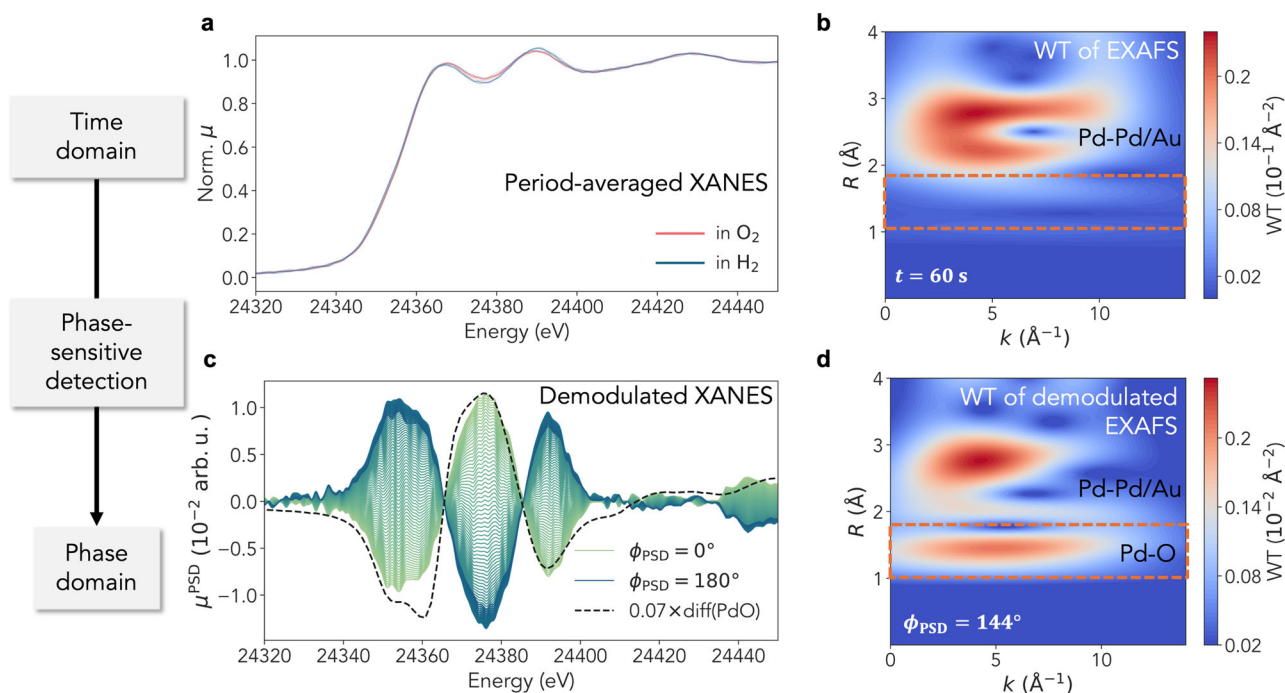


Fig. 2 | Sensitivity enhancement in ME-XAS. a Time-resolved ME-XANES spectra after period-averaging; **b** Wavelet transform (WT) of EXAFS in time domain at the end of O₂ half cycle of 60 s; **c** Demodulated XANES spectra obtained using PSD method after period-averaging shown at different phase angles ranging from 0° to

180°. A dashed line shows a scaled ($\times 0.07$) difference spectrum between Pd oxide (bulk) and the Pd-Au steady state spectrum after the modulation at the room temperature; **d** WT in k -space and r -space for demodulated spectra with highest change in absorption (at $\phi_{\text{PSD}} = 144^\circ$) showing a clear Pd-O bond scattering.

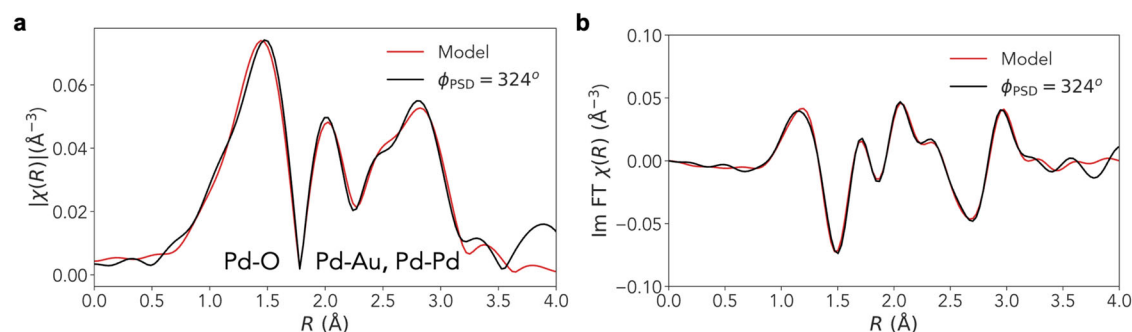


Fig. 3 | EXAFS analysis of demodulated spectrum. **a** The demodulated spectrum at $\phi_{\text{PSD}} = 324^\circ$ (black), and the model (red) obtained by using fit using Pd-O, Pd-Pd and Pd-Au scattering paths. **b** Corresponding imaginary part of Fourier transformed EXAFS spectrum (black) and the model (red).

contribution from Pd-O at $R = 1.5 \text{ \AA}$ in r -space, confirmed by the quantitative analysis (vide infra), in addition to Pd-Pd and Pd-Au. While the changes due to Pd oxide formation are clearly visible in phase domain, time-resolved XAS spectra, which are dominated by “spectators”, show only a minor contribution of Pd-O scattering (see Pd-O signature in Fourier transformed r -space EXAFS spectra Supplementary Fig. 1 in Supplementary Note 2). Such small contributions are very difficult to validate and separate from the artifacts of the EXAFS data processing involving subtracting the isolated-atom background (μ_0). Hence, demodulated EXAFS spectra show much higher sensitivity to surface formation of Pd oxide as compared to period-averaged time-resolved EXAFS spectra (Supplementary Fig. 1), where spectator-dominated contributions overshadow the relatively weak signals from Pd oxide. Next, we ask: Where are these 7% of Pd absorbers located and what are their local composition as well as transformation kinetics?

Local structure of restructuring species

To further investigate the information captured by demodulated EXAFS spectra, a complete structural model was obtained from the theoretical fit using Pd-O, Pd-Pd and Pd-Au photoelectron scattering paths (Fig. 3). The standard EXAFS equation is used to fit the demodulated spectra, albeit using a scaling correction (see Supplementary Note 1). While both phase angles of 144° and 324° (i.e., $144^\circ + 180^\circ$) show maximum contrasts for Pd oxide and result in equivalent demodulated spectra in magnitude, we chose the demodulated spectrum corresponding to the phase angle of $\phi_{\text{PSD}} = 324^\circ$ for fitting using the scattering paths from PdO sub-lattice as well as Pd-Au alloy lattice. A typical fitting model used for analysis of multicomponent systems by EXAFS, used for steady state EXAFS (Supplementary Note 3 and Supplementary Fig. 2), that contains a sum of all paths, when applied to demodulated EXAFS results in unrealistic interatomic spacing in the Pd-Au alloy structure. König et al. showed that for structural modeling using demodulated EXAFS, a differential model is more appropriate²⁸. Hence, we used a differential model with positive Pd-O scattering path added to the total theoretical EXAFS model, and rest of the scattering contributions—subtracted from it as shown in Table 1. The quantification of relative coordination number (N_{rel}) in Table 1 was carried out using Eq. (2):

$$N_{\text{rel}} = \frac{N_{\text{experimental}}^{\text{PSD}}}{N_{\text{theoretical}}} = \text{surface composition}, \quad (2)$$

where $N_{\text{experimental}}^{\text{PSD}}$ refers to the fit value obtained by EXAFS analysis of μ^{PSD} as shown in Fig. 4. $N_{\text{theoretical}}$ values are obtained from bulk PdO and Pd-Au alloy lattices.

The relative coordination of Pd-O with respect to its bulk counterpart (CN=4) indicates that the fraction of Pd atoms contributing to the modulated Pd-O bonds is 7.2% of all Pd atoms, which is also similar

Table 1 | EXAFS fitting parameters of demodulated spectra at $\phi_{\text{PSD}} = 324^\circ$ using a differential EXAFS model

$$\text{of } \chi_{\phi=324^\circ}^{\text{PSD}} = \chi_{\text{PdO}} - \chi_{\text{PdPd(PdO)}} - (\chi_{\text{PdAu}} + \chi_{\text{PdPd}})$$

	PdO		PdAu	
	Pd-O	Pd-Pd	Pd-Pd	Pd-Au
N	0.29	0.12	0.33	0.58
N_{rel}	7.2%	3.0%	2.7%	4.8%
$R(\text{\AA})$	1.96	2.95	2.68	2.73

to the fraction (7%) of S_2 species extracted using spectral decomposition of time-resolved XAS using multivariate curve resolution–alternating least squares (MCR-ALS) analysis (Supplementary Note 4 and Supplementary Fig. 3–7). Using EXAFS analysis (Supplementary Fig. 6b) of MCR-ALS obtained pseudo-species (their XANES data are shown in Supplementary Fig. 6a), we hypothesize that species labeled as S_2 is Pd oxide dominated, and species S_1 and S_3 are heterogeneous mixtures of Pd ensembles, Pd oxide and larger Pd-clusters. Approximately 3–5% of Pd atoms periodically make and break the Pd-Pd and Pd-Au bonds (out of the total number of Pd atoms in the Pd-Au alloy) with contracted interatomic spacing compared to that expected by Vegard’s law. An agreement with the demodulated XANES based (7%) fraction further reinforces the quantitative contribution of these surface species. Furthermore, additional insights about the mechanism of Pd restructuring resulting in Pd-Au and Pd-Pd scattering can be gained from the phase and time-dependent signal attenuation of each scattering path.

Dynamics of restructuring

In a modulated experiment, the observed phase delays in the reaction product with respect to the applied stimulus frequency provides a pathway to obtain the kinetic response of each species³⁶. Hence, the phase delay ($360^\circ - \phi_{\text{PSD}}$) between the Pd-Pd scattering, Pd-Au scattering and that of the Pd-O scattering from PdO_x species may hold a clue to the mechanism of the cyclic changes in the surface composition of the catalyst. Figure 4a and Supplementary Fig. 8 show a 2D map of phase-dependent signal attenuation in demodulated EXAFS as a function of phase angle (ϕ_{PSD}), where the maxima of the Pd-O scattering contribution are observed at 144° and 324° . With the individual contribution of each scattering path obtained in the structural model for $\phi_{\text{PSD}} = 324^\circ$, respective phase dependent signal attenuation for each path can be calculated provided the paths are well separated in FT EXAFS, as is the case with the Pd-O shell which is contained within the r -range of 1.1–1.7 \AA (denoted by dotted rectangle in Fig. 4a). Within the limited spatial resolution of $\delta r = 0.15 \text{ \AA}$ (given by the condition:

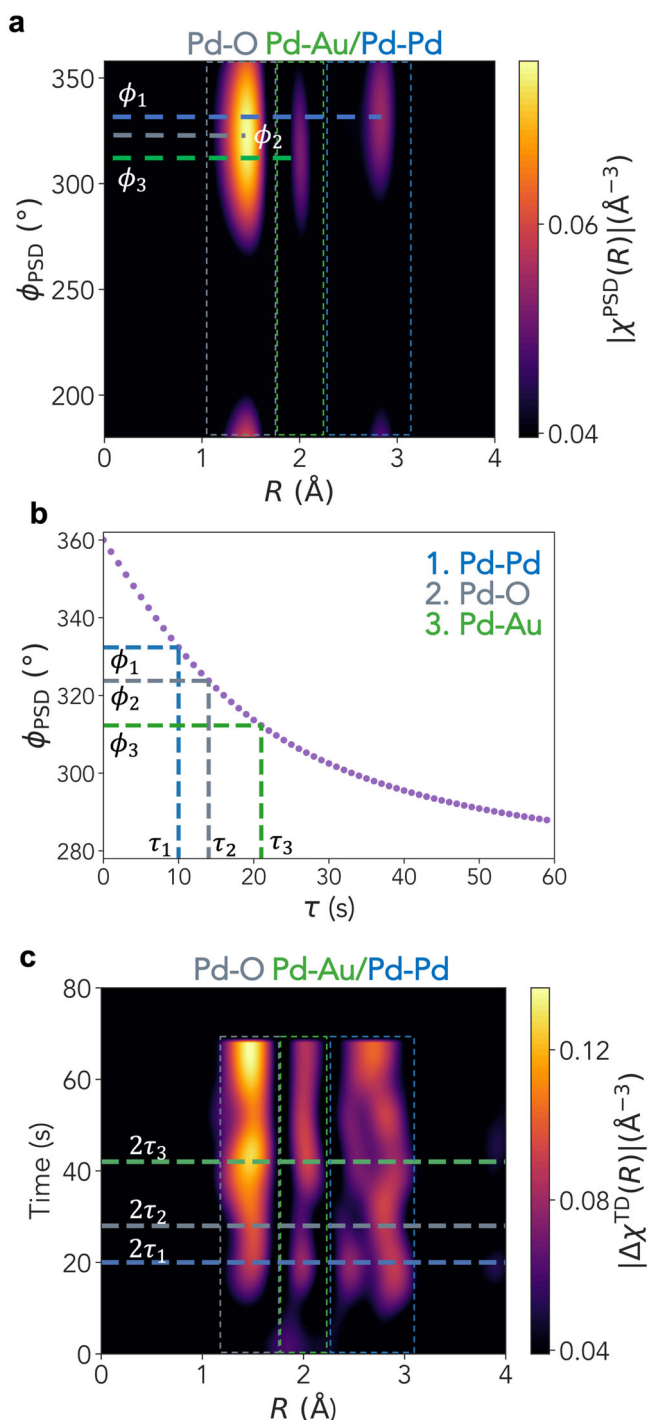


Fig. 4 | Phase-resolved and time-resolved Fourier Transformed EXAFS spectra. **a** 2D map of demodulated intensity attenuation in phase domain representing the relative phase lag between corresponding scattering paths. Based on the fitting of Pd-O, Pd-Pd and Pd-Au scattering paths, respective shells of dominant scattering contribution were selected (shown as rectangles) to calculate phase delays (Pd-O: 1.1–1.7 Å, Pd-Au: 1.8–2.2 Å, Pd-Pd: 2.3–3.1 Å shown in gray, green and blue colors, respectively). **b** The relationship between phase angle (ϕ_{PSD}) and the kinetic time constant (τ): $|\tan(\phi_{\text{PSD}})| = \omega\tau$. **c** 2D map of denoised data showing time-dependent evolution of difference spectra $\Delta\chi^{\text{TD}}(R)$ obtained after the subtraction of the mean absorption spectrum in H_2 [$\mu(t) - \mu_{\text{H}_2}^{\text{avg}}$].

$\delta r = \pi/(2k_{\text{max}})^{37}$, with the $k_{\text{max}} = 10.5 \text{\AA}^{-1}$, Pd-Pd scattering path from the Pd oxide lattice and the Pd-Au lattice cannot be reliably separated. Hence the r -range of 2.3–3.1 Å is assigned to the total Pd-Pd scattering

contributions. For the r -range of 1.8–2.2 Å, a dominant contribution arises from the left lobe of the Pd-Au doubler^{7,35} of Pd-Au scattering path and therefore is assigned in the Pd-Au. Figure 4a shows the phase delay, with respect to periodic gas pulse fronts represented by the 360° angle, of each scattering shell indicating that the maxima of Pd-Pd signal appears at $\phi_{\text{PSD}}^{\text{PdPd}} = 332^{\circ} \pm 1^{\circ}$, whereas Pd-O and Pd-Au lag with maxima at $\phi_{\text{PSD}}^{\text{PdO}} = 324^{\circ} \pm 1^{\circ}$ and $\phi_{\text{PSD}}^{\text{PdAu}} = 312^{\circ} \pm 1^{\circ}$, respectively. These phase lags identified by PSD provide the scattering paths as a proxy to identify the associated species with kinetically different responses which in this case can be assigned to least two distinct species, with PdO_x (containing Pd-O scattering) and surface Pd species (containing Pd-Pd and Pd-Au scattering).

To quantify the kinetics of Pd oxide formation and Pd-Au restructuring at the surface of Pd-Au bimetallic nanoparticles, we utilize a linear response model^{22,38}, where the phase delays reflect the average kinetics of species under the applied fixed frequency stimulus, as shown graphically in Fig. 4. The phase delays of Pd-Pd, Pd-O and Pd-Au, with respect to 360°, were found to correspond to time constants (τ) of 10, 14 and 21 s, respectively (Fig. 4b), indicating that, in the linear first-order kinetic approximation, the response of the surface species with residual Pd-Pd scattering is on average faster than other processes under the modulating conditions. However, since PSD analysis assumes a reversible transformation in each half period, the above-mentioned time constants represent an average kinetics information of formation and decomposition of each species. For a more interpretable time-dependent kinetic information, we developed a method to denoise the XAS spectra in time domain using nearest neighbor algorithm (kNN). More details about the denoising method are available in Supplementary Note 5 and Supplementary Figs. 9–12.

By examining the difference spectra: $\mu(t) - \mu_{\text{avg}}(\text{inH}_2)$ shown in Fig. 4c and time-dependent period-averaged EXAFS (Supplementary Note 5), reconstructed from the denoising of time-dependent information, we conclude that an increase in Pd-O signal is indeed dominant in the first half-period of O_2 . Furthermore, faster kinetics of Pd-Pd signal in the O_2 half-period is also evident in the time domain. Hence, the changes observed in Fig. 4c ($\tau_{\text{PdAu}} > \tau_{\text{PdO}} > \tau_{\text{PdPd}}$) support the information obtained via demodulated phase lag ($\phi_{\text{PSD}}^{\text{PdAu}} < \phi_{\text{PSD}}^{\text{PdO}} < \phi_{\text{PSD}}^{\text{PdPd}}$) seen in Fig. 4a. While the information in denoised time-domain EXAFS data reveals potential non-linearity in kinetics, the signal-to-noise ratio of XAS spectra using PSD is still superior to that of denoised time-domain spectra. Hence, we draw our quantitative conclusions about the local structure of Pd oxide using PSD based demodulated EXAFS analysis, as shown earlier.

Discussion

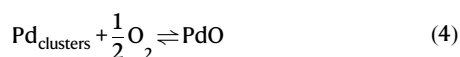
Here, we applied ME-XAS to elucidate dynamic structural changes in the Pd-Au bimetallic nanocatalysts and obtained robust evidence for the presence of Pd oxide on the surface of 30% Pd-Au. Under steady-state conditions, surface segregation of Pd in the form of thin Pd-rich islands in O_2 environment was observed in 25% Pd-Au bimetallic nanoparticles at a higher temperature of 400 °C under in-situ STEM⁸. At this elevated temperature, DFT studies showed favorable formation of $\text{PdO}(101)$ and $\text{Pd}_5\text{O}_4/\text{Au}(111)$ surfaces, and in-situ observations showed a transition from ordered surface to a rough surface in the presence of H_2 . However, given the bimetallic nature of 30% Pd-Au and partial coverage of Pd-islands on the surface, these surface oxides have been very challenging to determine until now, given the poor, if any, surface sensitivity of ensemble-averaged techniques³⁹. Previous work on pure Pd nanocatalysts has demonstrated the formation of thin surface oxide as well as a bulk oxide on the Pd crystal surface under oxidizing conditions³⁹. While our experiment clearly shows the reversible formation of Pd oxide, our analysis lacks sufficient resolution to exclude the possibility of multi-layered PdO_x formation on the surface,

therefore, we are hereby referring to Pd oxide as a surface and near-surface species.

In recent research, partial Pd oxide and Pt oxide surfaces were shown to have enhanced activity for CH₄ dissociation⁴⁰ and 2-propanol oxidation⁴¹, respectively. PdO surfaces are expected to be thermodynamically more favorable for certain catalytic reactions such as CH₄ dissociation. Rybakov et al.⁴² conducted theoretical calculations of multiple PdO surfaces and highlighted the need for a system containing undercoordinated Pd atoms along with PdO at the surface for higher reactivity. Depending on the PdO surface, the surface activation energy for the cleavage of the C–H bond in methane dissociation can be quite different, e.g., PdO(101) surface is much lower (0.7 eV) than that of PdO(100) and PdO(111) surface (1.4–1.6 eV)⁴⁰. Furthermore, the vacancies on PdO surfaces can lower the activation barrier even further. Theoretical modeling and experimental studies point toward the coexistence of Pd and PdO on the surface as key to increased activity and low temperature methane combustion. Our ME-XAS results indicate that a 30% Pd-Au bimetallic system with high Pd content at the surface would be able to fulfill these criteria, where Pd clusters at the surface undergo reversible redox Pd/PdO cycling. Since these bimetallic nanoparticles are dynamic in nature, Pd atoms on the surface can restructure as a result of pretreatment conditions, leading to formation of a diverse set of PdO surfaces. Our method is potentially useful for applications in catalysis using bimetallic Pd (or Pt)–Au alloys in which the stoichiometry of Pd and PdO on the surface as key to increased activity and low temperature methane combustion. Our ME-XAS results indicate that a 30% Pd-Au bimetallic system with high Pd content at the surface would be able to fulfill these criteria, where Pd clusters at the surface undergo reversible redox Pd/PdO cycling. Since these bimetallic nanoparticles are dynamic in nature, Pd atoms on the surface can restructure as a result of pretreatment conditions, leading to formation of a diverse set of PdO surfaces. Our method is potentially useful for applications in catalysis using bimetallic Pd (or Pt)–Au alloys in which the stoichiometry of Pd and PdO on the surface as key to increased activity and low temperature methane combustion.

ME-XAS also highlighted the presence of an “induction period” (as seen in Supplementary Figs. 6, 7) during the onset of O₂ and H₂ half pulse, indicating gas-phase reactions which precede changes in the nanocatalyst. H₂ dissociation at Pd clusters and subsequent reaction with surface oxygen atoms could explain the presence of such a delay. Similar induction periods have been shown to generate oxygen vacancies and active sites for dissociation of H₂ on the NiO interface⁴³. There is also a possibility of the restructuring as an independent process, which can in turn lead to dissociation and formation of Pd oxide at the surface. A plausible mechanism explaining the progression of these structural changes may also involve hydrogen-driven dissolution of Pd atoms from the PdO_x boundaries into the Au host, thus initiating the decomposition of the PdO_x phase via Pd–Au swapping⁴⁴. A difference in the driving forces of restructuring between the H₂ and O₂ atmosphere, is also evident from prior studies showing contiguous Pd surface segregation based restructuring in dilute Pd–Au alloys at higher temperature (above 200 °C) and planar Pd–Au surfaces (30% Pd) even at room temperature (RT)^{11,45}. While restructuring is known to be the dominant process at higher temperature under steady state conditions^{7,11}, our ME-XAS results show the presence of PdO_x and surface restructuring at 250 °C as well.

A kinetically faster process, such as Pd–Pd island formation could precede and/or support the Pd-oxide formation during the O₂ pulse. Pd–Pd scattering signals, if associated with Pd segregation, would result in formation of more contiguous Pd regions to be available on the surface for further Pd-oxide formation. As a result, Pd oxide, the reaction product of Pd-segregation in O₂ would lag the Pd clustering. Alternatively, the Pd–Pd signals could also be associated with Pd islands transforming to a Pd oxide lattice. The decrease of Pd–Pd scattering signal in the spectator dominated period-averaged spectra (after denoising) supports the latter scenario but does not exclude the former scenario from occurring at the surface.



Under H₂ atmosphere, period-averaged data (Supplementary Figs. 13, 14) in agreement with prior studies^{7,11,30}, show that Pd–Au restructuring signals are anti-correlated with Pd–O signal during the H₂ half pulse, indicating a Pd surface to subsurface migration. The changes in Pd–Au bonds in the demodulated spectra point towards Pd migration from surface to sub-surface, which was previously found to be the rate-determining step in the model surface of Pd–Au(100) and Pd–Au(111) surface where the proposed Pd–Au swapping was mediated by Au vacancies on the surface⁴⁴.

PSD provides a simpler method to quantify the kinetics by assuming linear and reversible transformation in each half-period, the time-domain information, and MCR-ALS results (Supplementary Fig. 7) show an asymmetric behavior in Pd clusters formation and Pd–Au restructuring during O₂ and H₂ pulse. As shown earlier, PSD-based demodulated EXAFS spectra were found to be, in the present case, superior in quality compared to the denoised time-domain EXAFS data, and therefore used for analysis of the local structure of Pd oxide. We also note (the details are given in Supplementary Note 6 and Supplementary Fig. 15) that mass-transport effects were estimated to be faster than the transformations observed in XAS data. While HRTEM and surface-sensitive probes such as X-ray photoelectron spectroscopy (XPS) provide complementary evidence to address the complexity of system (Supplementary Figs. 16–18), monitoring structural evolution via HRTEM under realistic in-situ conditions is relatively more limited. On the other hand, fast XAS instrumentation is a scarce resource. Another limitation of MES approach is that the period averaging-based sensitivity enhancement in ME-XAS would be applicable to the systems with quasi-reversible transformations only. ME-XAS-based dynamic surface characterization also makes it possible to tune the dynamic conditions, and control the surface characteristics e.g., coexistence of Pd and PdO on the surface, which is desirable for low-temperature methane combustion^{40,42}. Emerging developments with multi-frequency demodulation⁴⁶ and modeling of non-linear dynamics⁴⁷ of Pd–Au restructuring could also enable further refinement of studying the intermediate states and non-equilibrium surface sites available for catalysis during reaction conditions.

The knowledge of the structure and dynamics of surface and near-surface species, their local environment and spatial distribution is crucial for understanding the catalytic mechanisms. We showed that, by perturbing the 30% Pd–Au bimetallic nanocatalyst periodically by reacting gases, the contributions of the 3%–7% (of the total Pd amount) surface/near-surface species, namely, Pd, Pd–Au, and Pd oxides, were significantly amplified and detected in a modulation-excitation XAS (ME-XAS) experiment. The fractions of these species changed during the gas pulse application, from which not only the nature, but also the kinetics of surface transformations could be quantified. The formation of surface Pd oxides in O₂ pulse lagged with respect to the formation of Pd-rich regions near the Au surface due to O₂-induced Pd redistribution. During the H₂ pulse, the rapid Pd reduction was preceded by a pronounced induction period that we attribute to H₂ dissociation. These findings will inform theoretical models targeting the phenomena at bimetallic catalyst surfaces by accessing their dynamic (temporal) dimension. The time-dependent variations in the stoichiometry of the surface/near-surface oxides and metal ensembles and/or clusters, driven by the periodic perturbation of the catalyst by reacting gases, can provide dynamic control of the degree of oxidation/reduction of metals at/near the catalyst surface. We note also that denoising of time-resolved XAS data using more advanced machine learning methods, such as autoencoders for XAS, could be a promising avenue for improving our understanding of the restructuring dynamics and heterogeneities in bimetallic nanoparticles^{48,49}.

Methods

Chemicals

All chemicals were used as received without further purification. Hydrogen tetrachloroaurate trihydrate ($\text{HAuCl}_4 \cdot 3\text{H}_2\text{O}$, $\geq 99.9\%$), sodium borohydride (NaBH_4 , 99%), palladium nitrate ($\text{Pd}(\text{NO}_3)_2$, $\geq 99.99\%$), L-ascorbic acid ($\geq 99.0\%$), polyvinylpyrrolidone (PVP, $M_w \approx 55 \text{ kg mol}^{-1}$), styrene (contains 4-*tert*-butylcatechol as stabilizer, $\geq 99\%$), 2,2'-azobis(2-methylpropionamide) dihydrochloride (AAPH, 97%), and tetraethyl orthosilicate (TEOS, 98%) were purchased from Sigma-Aldrich, Merck. Absolute ethanol (EtOH) was purchased from KOPTEC. Ultrapure water (Millipore Milli-Q grade, MQ H_2O) with a resistivity of 18.2 M Ω cm was used in all experiments. All glassware for the Au nanoparticle (NP) synthesis was cleaned with fresh aqua regia (HCl/HNO_3 in a 3:1 volume ratio), rinsed with large amounts of water, and dried at 130 °C before usage.

RCT synthesis

The raspberry colloid templated (RCT) material containing $\text{Pd}_{31}\text{Au}_{69}$ NPs on silica was prepared via a multi-step colloidal procedure²⁹ consisting of Pd NP synthesis, attachment to thiol-functionalized polystyrene colloids to create raspberry colloids, Au overgrowth on the Pd NPs, assembly of the raspberry colloids in a colloidal crystal, infiltration of the interstitials with a silica sol-gel, and calcination to render a microporous silica framework with $\text{Pd}_{31}\text{Au}_{69}$ NPs at the pore walls.

Pd nanoparticles stabilized with PVP ligand were prepared using the procedure by Luneau et al.⁵⁰. In short, 4.3 g of PVP was dissolved in 75 mL of MQ H_2O . Next, 13.6 mg $\text{Pd}(\text{NO}_3)_2$ was added while stirring. The vial was placed in an ice bath under Ar atmosphere for 30 min before adding 1.5 mL of a 0.5 M NaBH_4 in MQ H_2O solution. The mixture was stirred for an additional 10 min in the ice bath, after which it was left to age for 48 h without stirring at RT. The procedure was repeated four times to make 300 mL Pd NP dispersion in total.

Raspberry colloids were prepared by attaching the Au NPs to the sacrificial polystyrene (PS) colloids ($d_{\text{PS}} = 393 \text{ nm}$). To 250 mL of PVP-stabilized Pd NPs 20 mL of thiol-functionalized PS colloids (5.0 wt.% in water) was added in a dropwise fashion under continuous stirring at 400 rpm. The pH was adjusted to 3 and the mixture was left to stir overnight. Next, the raspberry colloids were washed three times with MQ H_2O (centrifugation: 12,000 $\times g$ for 40 min) and redispersed in 20 mL of MQ H_2O (5.0 wt.% PS in water).

Au overgrowth on the Pd NPs attached to PS colloids was performed at low pH to ensure sufficiently slow reaction rates and selective growth on the Pd NPs⁵¹. 12 mL raspberry colloid dispersion (5.0 wt.% PS in water) was diluted to 250 mL in MQ H_2O . Next, 2.5 mL of 0.1 M HCl was added to lower the pH to ≈ 4 , while the reaction mixture was stirred at 400 rpm. Next, 7.0 mL of 10 mM HAuCl_4 and 7.0 mL of 40 mM ascorbic acid were added to obtain the $\text{Pd}_{31}\text{Au}_{69}$ NPs on PS. The mixture was left to react overnight. Next, the raspberry colloids were washed twice with 150 mL of MQ H_2O at 12000 $\times g$ for 45 min and finally redispersed in 12 mL of MQ H_2O (5.0 wt.% PS in water).

For the RCT preparation a total of three 4 mL aliquots of the raspberry colloid dispersion (5.0 wt.% PS in water) were dried in three separate conical vials at 65 °C in air. To each vial, $\approx 200 \mu\text{L}$ of pre-hydrolyzed TEOS solution (33 vol.% of a 0.10 M HCl in H_2O solution, 33 vol.% of ethanol, 33 vol.% of TEOS) was added to infiltrate the dried colloidal crystal. Thereafter, the sample was dried again at 65 °C. This step was repeated three times. The samples were calcined to remove PS colloids by heating them in static air from RT to 500 °C with 1.9 °C min^{-1} and held at 500 °C for 2 h and then cooled to RT over 3 to 4 h. Inductively coupled plasma - mass spectrometry (ICP-MS, Agilent Technologies 7700x) was used for compositional analysis. The metal composition of the NPs was 31 at.% Pd and 69 at.% Au, and the total metal loading on SiO_2 was 3.6 wt.%.

Experimental setup and mass transfer

MES XAS measurements could in principle be affected by mass-transfer phenomena at the scales of the entire setup, the reactor, and the macropores within the catalytic particles. The kinetic information can only be extracted from MES XAS data if the corresponding rates of chemical transformations are slower than the rate of gas transport at relevant spatio-temporal scales. Supplementary Note 6 gives the schematics of the MES experimental setup and provides the estimates of possible diffusion limitations. It is shown that they can be neglected in our case because the gas transport/exchange rates from the inlet perturbation to the gas composition at the sample surface can be considered fast with respect to the chemical transformations reported in this work.

Time-resolved quick-scanning X-ray absorption spectroscopy

The measurements at the Pd K-edge absorption were taken at the SuperXAS beamline of the Swiss Light Source, Paul Scherrer Institute, Switzerland. The setup of the ME-XAS experiments was described in details in the ref. 52. To obtain high-quality spectra, XAS data were collected in the total-fluorescence-yield mode with a time-resolution of 0.5 s per scan, using a PIPS detector. However, processed data is used with 1 s time interval. XAS in Pd foil, placed between the two ionization chambers located downstream of the reactor, was measured as reference to calibrate the energy scale. The reactor effluent was monitored during the experiments with an on-line Pfeiffer quadrupole mass-spectrometer connected to the outlet of the capillary reactor. In order to modulate the gases, two fast-acting three-way valves (Parker Series 9) synchronized with a single TTL signal actuating both simultaneously directly one flow to the reactor and another flow to the exhaust vent. Our setup imposes the switch in the inlet H_2 (or O_2) concentration with the nominal actuation time of 0.005 s. Using this setup a modulation excitation with period of 120 s with concentration modulation of the gas atmosphere using periodic pulse of 60 s 20% H_2 (in He) and 60 s 20% O_2 in (He) gas pulses.

ProQEXAFS⁵³ software was used to subtract the baseline of the pre-edge and to normalize the post-edge processing of all X-ray absorption spectra. EXAFS analysis was carried out using Fourier transform on k^2 -weighted EXAFS oscillations. The curve fitting of EXAFS spectra was conducted using the Artemis software of the Demeter program. Wavelet transform, MCR-ALS and PSD analyses were done using custom python scripts and open-source python packages: pyMCR and xraylarch.

Electron microscopy and elemental analysis

Ex-situ heat treatments in H_2 and O_2 were carried out mimicking the treatments conducted during the X-ray absorption measurements at the beamline. The pretreatments were carried out on special silicon nitrate (SiN) TEM grids, which were loaded to a quartz reactor. In total, three samples ex-situ samples were prepared. The first sample was pretreated in H_2 only. The sample was heated in 20% H_2 to 400 °C with a ramp of +10 °C min^{-1} . At 400 °C the sample was kept under isothermal conditions for 40 min. Cooling to RT was performed in helium. The second sample was heated in H_2 and subsequently in O_2 . First, the sample was heated in 20% H_2 to 400 °C with a ramp of +10 °C min^{-1} , kept at 400 °C for 40 min, and cooled in He. Subsequently, it was heated to 250 °C in 20% O_2 with 10 °C min^{-1} , kept at 250 °C for 1 h and cooled down in 20% O_2 . The third sample was pretreated in H_2 , and then heated O_2 followed by heating H_2 . First, the sample was heated in 20% H_2 in N_2 to 400 °C with a ramp of +10 °C min^{-1} , kept at 400 °C for 40 min, and cooled in He. Subsequently, it was heated to 250 °C in 20% O_2 with 10 °C min^{-1} , kept at 250 °C for 1 h after which reactor was flushed with He for 10 min before switching to 20% H_2 . The sample was treated for 1 h at 250 °C in H_2 , before cooling down to RT in the same gas atmosphere (20% H_2). More details are provided in Supplementary Note 7.

High-resolution HAADF-STEM imaging and STEM-EDX mapping were performed on the ex-situ samples using a double aberration-corrected Spectra300 microscope (Thermo Fisher Scientific) operated at 300 kV. The HAADF-STEM images were acquired using a beam convergence angle of 28.8 mrad, a collection angle range of 41–200 mrad, a camera length of 145 mm, spot size 5, images of 2048 × 2048 pixels and 1 μs dwell time. The EDX-maps were acquired using a beam convergence angle of 28.8 mrad, spot size 5, maps of 512 × 512 pixels, etc.

X-ray photoelectron spectroscopy

X-ray photoelectron spectroscopy (XPS) was performed using Thermo Scientific NEXSA XPS for the same set of heat-treated samples under ex-situ conditions. For each sample, approximately 5 mg of crushed catalyst powder was mounted onto a 0.5 cm × 0.5 cm piece of double-sided copper adhesive tape stuck on a Si wafer strip. The sample holder was loaded into the XPS chamber and pumped down until 10^{−7} mbar before irradiation with Al Kα radiation (1486.6 eV, generated by a 12 kV electron beam) with a 400 μm spot size and pass energy of 50 eV. Three spots were acquired for each sample to ensure that the data presented are representative of the sample. The acquired raw XPS data was fitted using Advantage software (Thermo Scientific) after calibrating the XPS data to the adventitious C 1s peak (assigned at 284.4 eV) and subtracting a Shirley background⁵⁴. Reference materials (Au/SiO₂ and Pd/SiO₂) were synthesized following ref. 50. More details are provided in Supplementary Note 8.

Reporting summary

Further information on research design is available in the Nature Portfolio Reporting Summary linked to this article.

Data availability

The data that support the findings of this study are available from the corresponding author upon request.

References

- Niu, Y. et al. Patterning the consecutive Pd(3) to Pd(1) on Pd(2)Ga surface via temperature-promoted reactive metal-support interaction. *Sci. Adv.* **8**, eabq5751 (2022).
- Huang, C., Chen, X., Xue, Z. & Wang, T. Effect of structure: A new insight into nanoparticle assemblies from inanimate to animate. *Sci. Adv.* **6**, eaba1321 (2020).
- Divins, N. J., Angurell, I., Escudero, C., Pérez-Dieste, V. & Llorca, J. Influence of the support on surface rearrangements of bimetallic nanoparticles in real catalysts. *Science* **346**, 620–623 (2014).
- Martin, A. J., Mitchell, S., Mondelli, C., Jaydev, S. & Pérez-Ramírez, J. Unifying views on catalyst deactivation. *Nat. Catal.* **5**, 854–866 (2022).
- Tao, F. & Salmeron, M. In situ studies of chemistry and structure of materials in reactive environments. *Science* **331**, 171–174 (2011).
- Vogt, C. & Weckhuysen, B. M. The concept of active site in heterogeneous catalysis. *Nat. Rev. Chem.* **6**, 89–111 (2022).
- Marcella, N. et al. Decoding reactive structures in dilute alloy catalysts. *Nat. Commun.* **13**, 832 (2022).
- Foucher, A. C. et al. Atomic-scale STEM analysis shows structural changes of Au–Pd nanoparticles in various gaseous environments. *J. Phys. Chem. C* **126**, 18047–18056 (2022).
- Serrer, M.-A. et al. Structural dynamics in Ni–Fe catalysts during CO₂ methanation—role of iron oxide clusters. *Cat. Sci. Technol.* **10**, 7542–7554 (2020).
- Han, Y.-F. et al. Au promotional effects on the synthesis of H₂O₂ directly from H₂ and O₂ on supported Pd–Au alloy catalysts. *J. Phys. Chem. C* **111**, 8410–8413 (2007).
- Luneau, M. et al. Enhancing catalytic performance of dilute metal alloy nanomaterials. *Commun. Chem.* **3**, 46 (2020).
- Gao, F. & Goodman, D. W. Pd–Au bimetallic catalysts: understanding alloy effects from planar models and (supported) nanoparticles. *Chem. Soc. Rev.* **41**, 8009–8020 (2012).
- Lee, J. D. et al. Dilute alloys based on Au, Ag, or Cu for efficient catalysis: from synthesis to active sites. *Chem. Rev.* **122**, 8758–8808 (2022).
- Liu, L. & Corma, A. Bimetallic sites for catalysis: from binuclear metal sites to bimetallic nanoclusters and nanoparticles. *Chem. Rev.* **123**, 4855–4933 (2023).
- Gao, F., Wang, Y. & Goodman, D. W. Reaction kinetics and Polarization-Modulation Infrared Reflection Absorption Spectroscopy (PM-IRAS) investigation of CO oxidation over supported Pd–Au alloy catalysts. *J. Phys. Chem. C* **114**, 4036–4043 (2010).
- Gibson, E. K. et al. Restructuring of AuPd nanoparticles studied by a combined XAFS/DRIFTS approach. *Chem. Mater.* **27**, 3714–3720 (2015).
- Sharma, A. K., Mehara, P. & Das, P. Recent advances in supported bimetallic Pd–Au catalysts: development and applications in organic synthesis with focused catalytic action study. *ACS Catal.* **12**, 6672–6701 (2022).
- Zhou, C. et al. Dynamical study of adsorbate-induced restructuring kinetics in bimetallic catalysts using the PdAu(111) model system. *J. Am. Chem. Soc.* **144**, 15132–15142 (2022).
- Filez, M. et al. Kinetics of lifetime changes in bimetallic nanocatalysts revealed by quick x-ray absorption spectroscopy. *Angew. Chem. Int. Ed.* **57**, 12430–12434 (2018).
- Urakawa, A., Bürgi, T. & Baiker, A. Sensitivity enhancement and dynamic behavior analysis by modulation excitation spectroscopy: Principle and application in heterogeneous catalysis. *Chem. Eng. Sci.* **63**, 4902–4909 (2008).
- Ferri, D. et al. First steps in combining modulation excitation spectroscopy with synchronous dispersive EXAFS/DRIFTS/mass spectrometry for in situ time resolved study of heterogeneous catalysts. *Phys. Chem. Chem. Phys.* **12**, 5634–5646 (2010).
- Urakawa, A., Bürgi, T. & Baiker, A. Kinetic analysis using square-wave stimulation in modulation excitation spectroscopy: Mixing property of a flow-through PM-IRRAS cell. *Chem. Phys.* **324**, 653–658 (2006).
- Chiarello, G. L. & Ferri, D. Modulated excitation extended X-ray absorption fine structure spectroscopy. *Phys. Chem. Chem. Phys.* **17**, 10579–10591 (2015).
- Müller, P. & Hermans, I. Applications of modulation excitation spectroscopy in heterogeneous catalysis. *Ind. Eng. Chem. Res.* **56**, 1123–1136 (2017).
- Ferri, D., Newton, M. A. & Nachtegaal, M. Modulation excitation x-ray absorption spectroscopy to probe surface species on heterogeneous catalysts. *Top. Catal.* **54**, 1070–1078 (2011).
- Vogt, C. et al. Unravelling structure sensitivity in CO₂ hydrogenation over nickel. *Nat. Catal.* **1**, 127–134 (2018).
- Vogt, C. et al. Dynamic restructuring of supported metal nanoparticles and its implications for structure insensitive catalysis. *Nat. Commun.* **12**, 7096 (2021).
- König, C. F., van Bokhoven, J. A., Schildhauer, T. J. & Nachtegaal, M. Quantitative analysis of modulated excitation X-ray absorption spectra: enhanced precision of EXAFS fitting. *J. Phys. Chem. C* **116**, 19857–19866 (2012).
- van der Hoeven, J. E. S. et al. Entropic control of HD exchange rates over dilute Pd-in-Au alloy nanoparticle catalysts. *ACS Catal.* **11**, 6971–6981 (2021).
- Guan, E. et al. New role of Pd hydride as a sensor of surface Pd distributions in Pd–Au catalysts. *ChemCatChem* **12**, 717–721 (2019).
- Silva, T. A. et al. From AuPd nanoparticle alloys towards core-shell motifs with enhanced alcohol oxidation activity. *ChemCatChem* **15**, e202300180 (2023).
- Knudsen, J. et al. Stroboscopic operando spectroscopy of the dynamics in heterogeneous catalysis by event-averaging. *Nat. Commun.* **12**, 6117 (2021).

33. Smolentsev, G., Guilera, G., Tromp, M., Pascarelli, S. & Soldatov, A. V. Local structure of reaction intermediates probed by time-resolved x-ray absorption near edge structure spectroscopy. *J. Chem. Phys.* **130**, 174508 (2009).
34. Wang, Q., Hanson, J. C. & Frenkel, A. I. Solving the structure of reaction intermediates by time-resolved synchrotron x-ray absorption spectroscopy. *J. Chem. Phys.* **129**, 234502 (2008).
35. Timoshenko, J., Keller, K. R. & Frenkel, A. I. Determination of bimetallic architectures in nanometer-scale catalysts by combining molecular dynamics simulations with x-ray absorption spectroscopy. *J. Chem. Phys.* **146**, 114201 (2017).
36. Marchionni, V., Ferri, D., Krocher, O. & Wokaun, A. Increasing the sensitivity to short-lived species in a modulated excitation experiment. *Anal. Chem.* **89**, 5801–5809 (2017).
37. Frenkel, A. I. et al. Direct separation of short range order in intermixed nanocrystalline and amorphous phases. *Phys. Rev. Lett.* **89**, 285503 (2002).
38. Xu, W. et al. Approach to electrochemical modulating differential extended X-ray absorption fine structure. *J. Synchrotron Radiat.* **29**, 1065–1073 (2022).
39. Chee, S. W., Arce-Ramos, J. M., Li, W., Genest, A. & Mirsaidov, U. Structural changes in noble metal nanoparticles during CO oxidation and their impact on catalyst activity. *Nat. Commun.* **11**, 2133 (2020).
40. Kinnunen, N. M., Hirvi, J. T., Suvanto, M. & Pakkanen, T. A. Role of the interface between Pd and PdO in methane dissociation. *J. Phys. Chem. C* **115**, 19197–19202 (2011).
41. Paredis, K. et al. Structure, chemical composition, and reactivity correlations during the in situ oxidation of 2-Propanol. *J. Am. Chem. Soc.* **133**, 6728–6735 (2011).
42. Rybakov, A. A., Bryukhanov, I. A., Trubnikov, D. N., Todorova, S. & Larin, A. V. Partial Palladium oxidation over various oxide supports for a higher reactivity of PdO with respect to CH₄. *J. Phys. Chem. C* **126**, 13132–13146 (2022).
43. Rodriguez, J. A., Hanson, J. C., Frenkel, A. I., Kim, J. Y. & Perez, M. Experimental and theoretical studies on the reaction of H₂ with NiO: role of O vacancies and mechanism for oxide reduction. *J. Am. Chem. Soc.* **124**, 346–354 (2002).
44. Kim, H. Y. & Henkelman, G. CO adsorption-driven surface segregation of Pd on Au/Pd bimetallic surfaces: role of defects and effect on CO oxidation. *ACS Catal.* **3**, 2541–2546 (2013).
45. Saint-Lager, M.-C. et al. Oxygen-induced changes of the Au₃₀Pd₇₀(110) surface structure and composition under increasing O₂ pressure. *J. Phys. Chem. C* **122**, 22588–22596 (2018).
46. De Coster, V., Srinath, N. V., Yazdani, P., Poelman, H. & Galvita, V. V. Modulation engineering: stimulation design for enhanced kinetic information from modulation-excitation experiments on catalytic systems. *ACS Catal.* **13**, 5084–5095 (2023).
47. Owen C. J., et al. Unraveling the catalytic effect of hydrogen adsorption on Pt nanoparticle shape-change. *arXiv preprint arXiv:230600901* (2023).
48. Routh, P. K., Liu, Y., Marcella, N., Kozinsky, B. & Frenkel, A. I. Latent representation learning for structural characterization of catalysts. *J. Phys. Chem. Lett.* **12**, 2086–2094 (2021).
49. Routh, P. K., Marcella, N. & Frenkel, A. I. Speciation of nanocatalysts using X-ray absorption spectroscopy assisted by machine learning. *J. Phys. Chem. C* **127**, 5653–5662 (2023).
50. Luneau, M. et al. Dilute Pd/Au alloy nanoparticles embedded in colloid-templated porous SiO₂: stable Au-based oxidation catalysts. *Chem. Mater.* **31**, 5759–5768 (2019).
51. van der Hoeven, J. E. S. et al. Structural control over bimetallic core-shell nanorods for surface-enhanced Raman Spectroscopy. *ACS Omega* **6**, 7034–7046 (2021).
52. Müller, O., Nachttegaal, M., Just, J., Lützenkirchen-Hecht, D. & Frahm, R. Quick-EXAFS setup at the SuperXAS beamline for in situ X-ray absorption spectroscopy with 10 ms time resolution. *J. Synchrotron Radiat.* **23**, 260–266 (2016).
53. Clark, A. H., Imbao, J., Frahm, R. & Nachttegaal, M. ProQEXAFS: a highly optimized parallelized rapid processing software for QEXAFS data. *J. Synchrotron Radiat.* **27**, 551–557 (2020).
54. Chastain, J. & King, R. C. Jr Handbook of X-ray photoelectron spectroscopy. *Perkin-Elmer Corp.* **40**, 221 (1992).

Acknowledgements

This project was primarily supported by Integrated Mesoscale Architectures for Sustainable Catalysis (IMASC), an Energy Frontier Research Center funded by the US Department of Energy, Office of Science, Office of Basic Energy Sciences, Award No. DE-SC0012573. SP acknowledges the iCSI (Industrial Catalysis Science and Innovation) Centre for Research based Innovation, which receives financial support from the Research Council of Norway under contract no. 237922. KRGL acknowledges financial support from the Agency for Science, Technology and Research (A*STAR) Singapore National Science Scholarship (PhD). The Swiss Light Source is acknowledged for the provision of beamtime at the SuperXAS beamline. JESvdH acknowledges funding from the NWO Veni project with project number VI.Veni.212.046 which is financed by the Dutch Research Council (NWO), and funding for access to the TFS Spectra300 at EM Utrecht from the Netherlands Electron Microscopy Infrastructure (NEMI), project number 184.034.014, part of the National Roadmap and financed by the Dutch Research Council.

Author contributions

E.R., A.I.F. and P.K.R. proposed the research. P.K.R., S.P., E.R., M.N., A.H.C. and A.I.F. conducted X-ray absorption spectroscopy and reaction measurements. J.E.SvdH. synthesized the samples, advised by J.A. K.R.G.L. conducted the XPS measurements and J.E.SvdH. performed electron microscopy on the samples. P.K.R. performed data analysis, advised by A.I.F. P.K.R., E.R. and A.I.F. wrote the manuscript with input from all authors.

Competing interests

The authors declare no competing interests.

Additional information

Supplementary information The online version contains supplementary material available at <https://doi.org/10.1038/s41467-024-51068-4>.

Correspondence and requests for materials should be addressed to Anatoly I. Frenkel.

Peer review information *Nature Communications* thanks Lichen Liu, Jihan Zhou, and the other, anonymous, reviewers for their contribution to the peer review of this work. A peer review file is available.

Reprints and permissions information is available at <http://www.nature.com/reprints>

Publisher's note Springer Nature remains neutral with regard to jurisdictional claims in published maps and institutional affiliations.

Open Access This article is licensed under a Creative Commons Attribution-NonCommercial-NoDerivatives 4.0 International License, which permits any non-commercial use, sharing, distribution and reproduction in any medium or format, as long as you give appropriate credit to the original author(s) and the source, provide a link to the Creative Commons licence, and indicate if you modified the licensed material. You do not have permission under this licence to share adapted material derived from this article or parts of it. The images or other third party material in this article are included in the article's Creative Commons licence, unless indicated otherwise in a credit line to the material. If material is not included in the article's Creative Commons licence and your intended use is not permitted by statutory regulation or exceeds the permitted use, you will need to obtain permission directly from the copyright holder. To view a copy of this licence, visit <http://creativecommons.org/licenses/by-nc-nd/4.0/>.

© The Author(s) 2024